IEEE Access
Multidisciplinary | Rapid Review | Open Access Journal

Received April 5, 2020, accepted April 17, 2020, date of publication April 21, 2020, date of current version May 6, 2020.

Digital Object Identifier 10.1109/ACCESS.2020.2989369

Nucleus Segmentation of Cervical Cytology Images Based on Depth Information

TAO WANG[1,2,3], JINJIE HUANG[1,2], DEQUAN ZHENG[3], AND YONGJUN HE[1], (Member, IEEE)

[1]School of Computer Science, Harbin University of Science and Technology, Harbin 150080, China
[2]Key Laboratory of Advanced Manufacturing and Intelligent Technology, Ministry of Education, Harbin 150080, China
[3]Network and Education Technology Center, Harbin University of Commerce, Harbin 150028, China

Corresponding author: Jinjie Huang (jjhuang@hrbust.edu.cn)

This work was supported in part by the National Natural Science Foundation of China under Grant 61305001, and in part by the Natural Science Fund Project of Heilongjiang under Grant F201222.

ABSTRACT In cervical cancer screening, accurate segmentation of cervical nucleus is a key part in the early diagnosis of cervical cancer. However, the cervical nucleus segmentation faces many great challenges owing to the overlapping cervical cells, uneven staining and poor contrast of cervical cytology smear images. In this paper, a tree domain structure and screening algorithm based on depth-first searching strategy are proposed to obtain candidate nucleus regions according to the annular clustering characteristics of nucleus depth information in cervical cytology images. Then, the candidate nucleus regions are finely segmented with an iterative level set algorithm based on adaptive radius morphological dilation. Experimental results are evaluated on the ISBI2015 public dataset. The performance of the proposed nucleus segmentation algorithm is higher than that of the state-of-the-art methods in terms of positive predictive value, negative predictive value, precision, recall of the cervical nucleus segmentation.

INDEX TERMS Cervical cancer screening, cervical cell, nucleus segmentation, tree domain structure.

I. INTRODUCTION

Cervical cancer is one of the four common cancers in the world. Approximately 266,000 people die of cervical cancer each year [1], [2]. However, the early canceration of cervical cells has no visible symptoms of physical malaise or physiological reaction that are easily perceptible. A pathologist generally observes cervical cytology smears through a microscope and identifies abnormal cells on the basis of the morphology of cervical cells and their nuclei using the Papanicolaou (PAP) test. The PAP test is an effective means of detecting early cervical carcinogenesis through manual screening.

Screening of cervical cancer cell is a time-consuming task and highly repetitive work that requires the utmost attention of a pathologist. Even an experienced pathologist may have screening errors due to fatigue and decreased attention after long-term working. Therefore, a computer-aided diagnosis (CAD) system is needed to assist pathologists in the segmentation and identification of cervical cells.

The associate editor coordinating the review of this manuscript and approving it for publication was Mohamed Elhoseny.

The application of CAD reduces the workload of pathologists, allowing them to focus more on the diagnosis and identification of abnormal cervical cells. Consequently, the accuracy of PAP is improved, and the mortality of cervical cancer is reduced. In response to the lack of pathologists in developing countries, CAD improves the diagnostic efficiency of pathologists. When cervical cells have pathological changes, they show nucleus atypia, such as nucleus enlargement, hyperchromatism, membrane thickening and irregularity. From these nucleus atypia, the CAD system can be used to segment the nucleus and conclude whether cells have lesions or not. As the first step of the CAD system for cancer cell screening, accurate segmentation of the nucleus has a positive influence on the recognition of cervical cancer cell.

Cervical nucleus segmentation involves certain challenges, such as the overlapping cervical cells, uneven staining, poor contrast, and presence of neutrophils. Many scholars have conducted extensive research in the nucleus segmentation, and some algorithms have been proposed, including threshold methods [3]–[5], watershed methods [16]–[19], morphological algorithms [6]–[8], deformable models [9]–[13], template-matching algorithms [14], [15], graph-based

segmentation algorithms [20], [21], region-based methods [22]–[25], clustering methods [26]–[29], and neural network methods [30]–[32].

The threshold method is a traditional method used in medical image segmentation, and it has low computational complexity. In a previous study, Santosh *et al.* utilized the fuzzy binarization algorithm to complete binary image segmentation, and then detected the candidate arrows by the connected component principle [3]. Phoulady *et al.* adopted an iterative threshold method to generate the candidate nuclei [4]. Lee *et al.* proposed an adaptive threshold method to segment cervical nuclei [5]. In the overlapping cell images, the threshold-based method often makes errors in segmentation, because the overlapping part of the cytoplasm is dark, and the intensity is close to that of the nucleus.

Watershed segmentation is a classical image segmentation algorithm. In some studies, the watershed algorithm based on marker control has shown a good effect on nucleus segmentation. Jung *et al*. utilized a marker extraction scheme based on the H-minima transform to obtain the optimal segmentation result [16]. Gençtav *et al.* adopted a multi-scale marker watershed method to segment the nuclei, and utilized a hierarchical clustering method to classify the nucleus and cytoplasm regions [17]. Tareef *et al*. used the triangular transformation algorithm to extract cell clumps and combined the simple linear iterative clustering (SLIC) algorithm with the marker-based watershed algorithm to extract the candidate nuclei [19]. The accurate extraction of marker is the biggest obstacle for the marker watershed algorithm, due to the uneven staining of the cell preparation process and the presence of neutrophils. Some scholars, like Plissiti *et al*. [6], [7], [18] and Tello-Mijares [8], utilized the morphological methods to extract nucleus marker.

Deformation model-based methods, such as active contour model (ACM), snake, and level set method, can extract object in medical images precisely. Hu *et al.* improved the ACM algorithm through appending a regional similarity term to the energy functional, which overcomes initialization problem of traditional algorithms [10]. Subsequently, the improved ACM algorithm was applied to the contour detection of nuclei. Plissiti *et al.* used the convex hull of the nucleus as the initial contour, and then utilized the Gradient Vector Flow (GVF) snack algorithm to refine the boundary of cervical nucleus [11]. Li *et al.* proposed radial gradient vector flow (RGVF) based on the GVF snake method to detect the boundary of cervical cells and nuclei, and obtained more accurate detection results for obscure boundaries [12]. To overcome topological constraint of the snake method, Husham *et al.* used the level set method to segment the nuclei [9]. The morphological method was adopted to detect the seed nodes for level set evolution. Subsequently, the level set algorithm based on the geometric deformation model was utilized to segment the nucleus boundary. In addition, Nosrati *et al.* used the star-shape prior based level set to segment the nuclei and cells in overlapping cervical cells, and obtained high experimental results on the ISBI2014 dataset [13]. The level set method has the advantages of not requiring explicit parameters and not being constrained by topology, but the algorithm has low calculation efficiency.

Chen *et al.* separated individual nuclei and adhesion nuclei by the template matching method [14]. First, a statistical model was obtained through the training dataset. Subsequently, the model was used to perform coarse segmentation of the nuclei. Bergmeir *et al.* utilized a template based on elliptical randomized Hough transform to identify the cervical nuclei [15]. The segmentation result of the template matching method is dependent on the representativeness of the training dataset. Obtain a representative training dataset is the biggest challenge faced by the method.

For graph-based image segmentation, Saha *et al.* used a priori knowledge of weighted circles to segment the nuclei, and obtained excellent results on the ISBI2014 dataset [20]. Zhang *et al.* utilized the local adaptive a graph cut method to segment the cervical nuclei, and obtained improved performance in the nucleus segmentation of abnormal cervical cells [21].

In recent years, region-based segmentation techniques have been explored in the field of cervical nucleus segmentation. Lu *et al.* [22] utilized the maximally stable extremal region (MSER) algorithm and nucleus ellipticity feature to identify and screen nuclei, and improved the algorithm in [23]. Oprisescu *et al.* applied region growth segmentation on the boundary detected by the Sobel operator [24]. Tello-Mijares *et al.* used mean-shift over-segmentation technology and region fusion algorithm to identify candidate nuclei [25]. The nucleus segmentation using a region-based method is susceptible to false positive nuclei in overlapping cervical cell images.

The clustering algorithm is an effective object segmentation method used by CAD system. Tello-Mijares *et al.* combined the multi-focus fusion algorithm with a mean-shift clustering segmentation algorithm to segment the best-focused cervical images [26], [27]. Fuzzy C-Means (FCM) algorithm and its improved algorithm were used extensively in segmenting brain magnetic resonance images. Saha *et al.* first adopted the FCM algorithm for overlapping cervical cytology image segmentation, which added a circular function to increase robustness [28]. In addition, they conducted further work on the basis of [28] and used MSER algorithm to adaptively calculate the spatial shape force threshold. As a result, the recall and accuracy rates were improved [29].

In recent years, neural network methods have achieved positive results in the field of medical image segmentation. Santosh *et al.* proposed a sequential classifier comprising a bidirectional long short-term memory classifier to detect annotated arrows [30]. Tareef *et al.* first performed super-pixel segmentation of the cervical cell image using the SLIC algorithm, and used a convolutional neural network (CNN) to identify the nuclei and cell clusters [31]. Song *et al.* used the CNN algorithm to segment cervical cell images [32].

Among these methods, some were tested on the ISBI2015 public dataset, which was presented in the Second Extended

Depth of Field-based Overlapping Cervical Cell Segmentation organized by the IEEE International Biomedical Imaging Symposium in New York, USA in April 2015. On the basis of the ISBI 2015 public dataset, Lu proposed a nucleus segmentation method [33]. First, the SLIC method and edge detection algorithm were used to obtain a super-pixel boundary map of the cervical cytology image. The Gaussian mixture model and MSER algorithm were adopted to extract the cell clumps and candidate nuclei. The algorithm harvested high nucleus segmentation accuracy on the ISBI2015 dataset. However, the application of the SLIC algorithm produces oversegmented nuclei, which can reduce recognition accuracy.

On the ISBI2015 dataset, Phoulady *et al.* applied an iterative threshold algorithm to obtain the nucleus boundary on the cervical cytoplasm images [4]. Lee *et al.* proposed a window-based local adaptive threshold method to segment the cervical nuclei [5]. This algorithm reached high nucleus recognition accuracy, but the choice of size of the local window had a major influence on the segmentation results. Tareef *et al.* used the triangular transformation algorithm to extract the cell clumps, combined the SLIC algorithm with the marker-based watershed algorithm to extract the candidate nuclei, and adopted the level set algorithm to finely segment the candidate nuclei [19]. The algorithm has low computational complexity but produces over-segmented pseudo-nuclei, which can reduce the recognition accuracy. Song *et al.* [32] used the CNN algorithm to classify each pixel in a cervical cytology sample into three categories: background, cell clump, and nucleus. This method has improved the accuracy of nucleus extraction. However, the large number of parameters, the huge quantity of training data required, and the high computational complexity are all problems that cannot be ignored in the algorithm.

A cervical smear is usually with certain thickness. It is observed through a microscope as shown in Fig. 1(a). In the same field of view, as the microscope eyepiece moves, a stack of focal plane images can be captured, which are referred to herein as a *cervical cytology sample with depth information*, as shown in Fig. 1(b). Each cell is shown in a focused or defocused state on one focal plane, as shown in Fig. 1(c). The best focused state image of each cell in the sample is combined into an image called an extended depth of field (EDF) [40] image, as shown in Fig. 1(d).

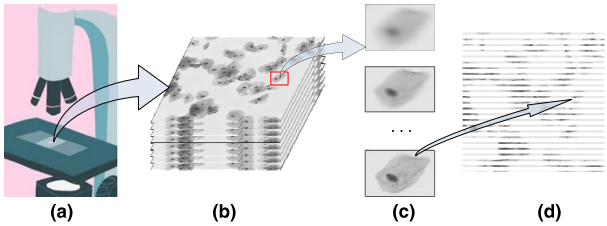

FIGURE 1. Cervical cytology samples with depth information and synthetic EDF images. (a) Microscopic observation of cervical cell smear. (b) Cervical cytology sample with depth information. (c) The focused and defocused states of a cell. The bottom image shows the focused state of the cell. (d) Synthetic EDF image from the best focused state of each cell.

Although the EDF image obtains the best focused state images of the cells in the cervical cytology sample, due to cell overlap, the EDF image is unable to present the best focused states of all cells simultaneously. Therefore, the EDF image has lost some information of the cells, while the cervical cytology samples with depth information preserve the total original information. When we perform a clustering of cervical cytology samples with depth information, an annular characteristic is appeared surrounding the area of a nucleus. In our study, we'll make use of these annular features to identify the nuclei and utilize the iterative level set algorithm based on adaptive radius morphological dilation to segment the nuclei finely.

The main contributions of our method presented in this paper are as follows: 1) compared with other nucleus segmentation algorithms, the proposed algorithm directly uses the depth information of the cervical cytology samples rather than the EDF images; 2) through constructing the tree domain structure of annular features after clustering of depth information, the nuclei can be accurately identified; 3) a novel iterative level set algorithm based on adaptive radius morphological dilation is proposed, which can find the optimal dilation radius adaptively and carry out the nucleus segmentation results accurately.

II. METHODS

The algorithm is mainly divided into three steps. The first step is cell clump recognition, which is to obtain the interesting regions of nucleus recognition. In the second step, approximate segmentation is performed by constructing the tree domain and screening the candidate nuclei based on the depth-first strategy to obtain the candidate nuclei in the cell clump. In the third step, fine segmentation and pseudo-nuclei removal are performed. The process of nucleus segmentation algorithm is shown in Fig.2.

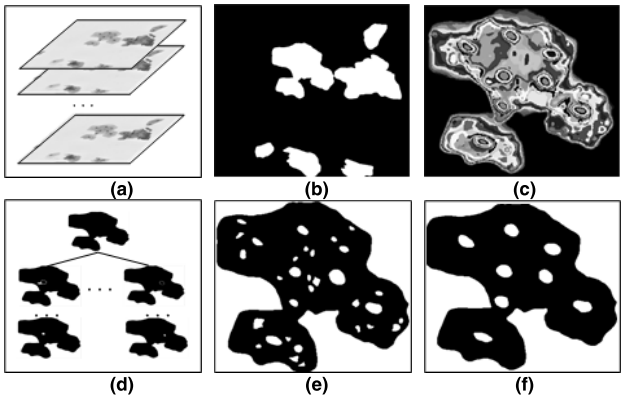

FIGURE 2. The process of nucleus segmentation algorithm. (a) Input images. (b) Cell clumps. (c) Interesting regions. (d) Tree-domain. (e) Candidate nuclei. (f) Nuclei.

A. CELL CLUMP RECOGNITION

To obtain the interesting region of nucleus recognition, our algorithm recognizes the cell clumps by FCM clustering algorithm. The FCM clustering algorithm was proposed by

Dunn [35] and Bezdk improved the algorithm in [36]. In this paper, we adopt Bezdk's FCM algorithm to segment the cervical cell clumps. Denote I as a cervical cytology sample consisted of N focal-plane images, I^s as the *s-th* focal-plane image ($s = 1, 2, \cdots, N$) and N as the total number of focal planes of a sample. Denote the gray value of the pixel at position i of the *s-th* focal-plane image as $gray_i^s$. Thus, N gray values of the position i of the cervical cytology sample can be expressed as a gray vector $X\_gray_i = [gray_i^1, gray_i^2, \ldots, gray_i^N]$, $(i = 1, 2, \ldots, P)$, where P is the total number of positions in the cervical cytology sample I. Now, we use the Bezdk's FCM algorithm to cluster the P gray vectors into three categories, corresponding to the nucleus, cytoplasm and background respectively. Denote V_k as the cluster centers, $(k = 1, 2, 3)$. The fuzzy partition matrix is defined as $U = [u_{ik}]_{K\times P}$, where $u_{ik}(1 \le i \le P, 1 \le k \le K, K = 3)$ represents the membership degree of the gray vector i to the category k, and the membership degree should satisfy (1) and (2).

$$u_{ik} \in [0, 1], \quad 1 \le i \le P, \ 1 \le k \le K \tag{1}$$

$$\sum_{k=1}^{K} u_{ik} = 1, \quad 1 \le i \le P \tag{2}$$

The objective function of the FCM algorithm is defined as (3), where d is the Euclidean distance of the gray vector X_gray_i and the cluster center v_k.

$$J(U, V) = \sum_{k=1}^{K}\sum_{i=1}^{P} (u_{ik})^2 d^2(X\_gray_i, v_k) \tag{3}$$

FCM is based on the minimization of the objective function. The cluster centers are updated by (4) iteratively.

$$v_k = \frac{\sum_{i=1}^{n} (X\_gray_i u_{ik}^2)}{\sum_{i=1}^{n} u_{ik}^2} \tag{4}$$

Afterwards, the membership degree matrix U is updated by (5).

$$u_{ik} = \frac{1}{\sum_{j=1}^{K} \left(\frac{||X\_gray_i - v_k||}{||X\_gray_i - v_j||} \right)^2} \tag{5}$$

Remarks: In actual cervical cytology images, the nucleus, cytoplasm, and background regions generally exhibit three typical levels in grayscale. We take the number of category $K = 3$ in FCM clustering so that the nucleus, cytoplasm and background regions can be recognized accordingly; on this basis, the nucleus regions and the cytoplasm regions are combined into cell clump regions, thus the cell clumps and the background regions can be separated. The cell clump recognition algorithm is shown in Algorithm 1.

Algorithm 1 Cell Clump Recognition Algorithm

Input: Cervical cytology sample I
Output: Cell clump mask image I_{Mask_clump}
Set $K = 3, \delta = 0.001, J\_last = 100000$
$[U, v] = init\_rand(I, K)$% Random initialization function
$X\_gray = trans(I)$ % Express I as gray vectors
while 1 **do**
  % Calculate the distance between X_gray_i and v_k.
  foreach $X\_gray_i \in X\_gray$ **do**
    foreach $v_k \in v$ **do**
      $dist = distance(X\_gray_i, v_k)$
    end
  end
  % Calculate the objective function J
  $J = cal\_J\ (U, dist)$
  if $abs(J\_last - J) < \delta$ **then**
    break
  else
    %Update U, v based on (4) and (5)
    $[U, v] = update(X\_gray, U, v)$
    $J\_last = J$
  end
end
% Find categories of gray vectors by largest membership value and produce the category mask image
$X\_cate = get\_cate(X\_gray, U)$
$mask\_cate = trans\_mask\ (X\_cate)$
%Perform a connected domain analysis to merge the nuclei and cytoplasm regions
$I_{Mask\_clump} = mask\_cate(mask\_cate)$

B. DISPERSION EFFECTS OF DEFOCUSING

The gray value of nuclei in the cervical cytology sample is small relative to the cytoplasm region. Traditional nucleus segmentation methods for cervical EDF images are based on gray value, boundary, and gradient features [4], [5], [19], [23], [33]. They can segment large contrast between nucleus and cytoplasm. However, the contrast of nucleus and cytoplasm is low due to uneven dyeing and insufficient light intensity. In this case, the nucleus is difficult to identify only by the features in the EDF image. Owing to the overlapping cells, EDF image may lose some best focused state information of some overlapping cells; whereas the cervical cytology samples with depth information can preserve the total original information. So, the use of depth information of the cervical cytology samples can segment the nuclei in lower contrast cervical cytology images, as shown in Fig.3.

The principle of optical imaging of the microscope, as shown in Fig. 4, indicates that the point A on the object plane OP forms a clear spot A' on the focal plane FP through the microscope L. As the focal plane moves, a clear spot cannot be formed on it, instead a blurred diffuse spot exists,

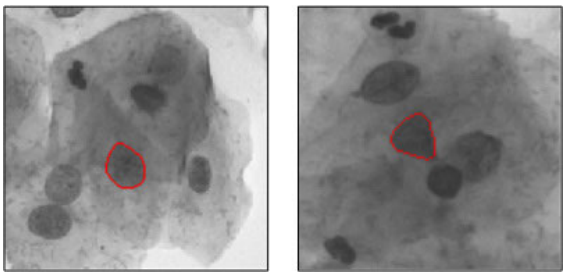

FIGURE 3. The lower contrast nuclei. The red lines are the nucleus boundary extracted by the depth information.

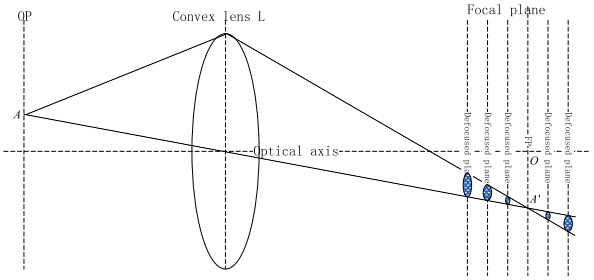

FIGURE 4. Principle of optical imaging.

such as the elliptical region with the textured background in Fig. 4.

The principle of Fourier optical imaging states that the defocusing process can be regarded as a process of continuous low-pass filtering of the focal plane, i.e., the convolution process of point spread function (PSF) and the focal plane.

The nucleus dispersion process can be described as (6),

$$\begin{aligned} \Omega_1 &= \Omega \otimes \sigma_1 \\ \Omega_2 &= (\Omega \otimes \sigma_1) \otimes \sigma_2 \\ &\cdots \\ \Omega_N &= ((\Omega \otimes \sigma_1) \otimes \ldots) \otimes \sigma_N \end{aligned} \tag{6}$$

where Ω denotes the focused nucleus, σ_N denotes the *N-th* disperse convolution kernel, and Ω_N denotes the disperse nucleus generated by N defocusing operations.

As the microscope eyepiece moves along the optical axis, different focal planes $F_1, F_2, \cdots, F_N$ can be obtained. Assume that there are 4 two-dimensional planes with a resolution of 50 $pix \times 50$ pix in the field of view, as shown in Fig. 5(a). The current focal plane of the nucleus is F_1 with an elliptical shape of semi-major axe 12 and semi-minor axe 10 respectively, located at the center of the field of view, as shown in Fig. 5(b). Assume that the gray value inside the nucleus in F_1 is 255, the gray value of other positions is 0, the disperse kernel is a Gaussian kernel with a size of 5*5, and the scale parameter σ is 1.5. Take the sample points A, B, C outside the nucleus and the sample points A', B', C' inside the nucleus with 2 pixels distance to the boundary, as shown in Fig. 5(b).

The gray value of the sample point i on the planes $F_1, F_2, \cdots, F_N$ constitute the depth information vector $[g_1^i, g_2^i, \cdots, g_N^i]$, where g_s^i represents the gray value of the position i of the plane s, and N represents the number of

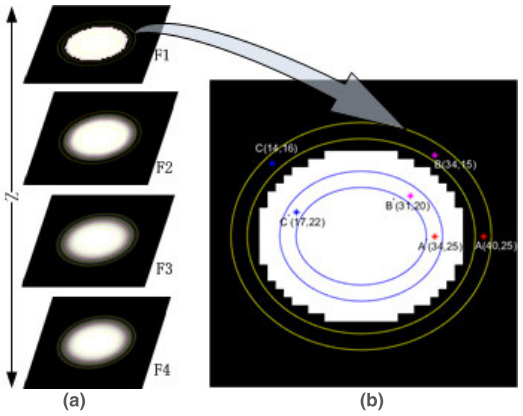

FIGURE 5. The dispersing process of nucleus. (a) The dispersing process of nucleus, and F_1 is the focal plane of the nucleus; (b) F_1 focal plane and sample points selection. The sample points A, B, C coordinates are (40, 25), (34, 15), (14, 16), and the sample points A', B', C' coordinates are (34, 25), (31, 20), (17, 22). The region surrounded by the blue ellipse is the annular region at a distance of 2 from the boundary of the nucleus. The region enclosed by the yellow ellipse is the outer nucleus annular region at a distance of 2 from the nuclear boundary.

planes. The distance between the two sample points i and j is defined as (7) based on the depth information of the sample.

$$d_{i,j} = \sqrt{\sum_{s=1}^{N} \left(g_s^i - g_s^j\right)^2} \tag{7}$$

The formula (7) is used to calculate the distance $d(\cdot)$ in the objective function formula (3) in the FCM algorithm. After clustering, the sample points with approximate gray values are divided into the same class, forming an annular region around the nucleus.

Due to the dispersion effect of defocusing, the gray level around the nucleus varies uniformly. The farther away from the nucleus, the more the gray level is decreased. Moreover, around the nucleus, the pixels with the same distance to the nucleus have approximate gray values. Therefore, the pixels farther away from the nucleus form an annular region with a larger radius around the nucleus, while the pixels closer to the nucleus form another annular region with a smaller radius, which is embedded in the large one.

In the example of Fig.5, the planes F_2, F_3, F_4 are obtained by the defocusing process. Together with the focal plane F_1, these planes comprise of the depth information samples under one field of view. For instance, the gray depth information of the six sample points in Fig.5 is $g^A = [0, 0, 0, 2]$, $g^B = [0, 15, 24, 25]$, $g^C = [0, 0, 7, 11]$, $g^{A'} = [255, 186, 141, 110]$, $g^{B'} = [255, 211, 172, 137]$, and $g^{C'} = [255, 208, 158, 123]$. After FCM clustering, sample points A, B, C are classified into the same cluster and located in the same annular region. So do the sample points A', B', C'. The focusing process is just the reverse of the defocusing process.

C. NUCLEUS APPROXIMATE SEGMENTATION

According to the annular structure generated in the nucleus defocusing process, we propose a nucleus segmentation

algorithm based on the clustering of nucleus depth information. The algorithm is mainly divided into three parts: 1) preprocessing and clustering; 2) constructing the tree domain structure based on clustering results; and 3) screening the candidate nuclei within the tree domain.

1) PREPROCESSING AND CLUSTERING

The sample is affected by various noises, which result in many noise points in the clustering image, as shown in Fig. 6(a). So, we utilize a median filter to denoise each focal plane. After denoising, the gray vector of index position i of sample I is (8),

$$X\_gray_i\_med = [gray_i^1\_med, \ldots, gray_i^N\_med] \quad (8)$$

where N is the number of focal planes. In cervical cell images, gray value of nucleus is less than the cytoplasm and background, and different types of nuclei have different gray value properties. In different types of nuclei, the nuclei of cervical intraepithelial neoplastic cells and cancer cells are hyperchromatic, and the nuclei of overlapping cells are more hyperchromatic than those of normal cervical cells and weaker than those of abnormal cervical cells. Therefore, we can utilize the clustering of gray value to obtain nuclei. The FCM clustering algorithm is used again and we cluster the cell clump regions with the number of clusters K = 30 to obtain the annular regions. Here, the FCM algorithm is different from its first use for cell clump recognition in the clustering objects, the number of cluster categories, and the clustering aim. The clustering results are illustrated in Fig. 6(b).

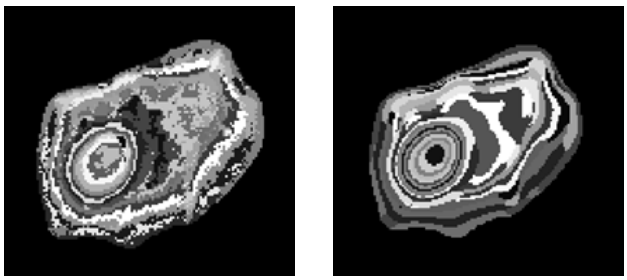

FIGURE 6. Clustering results based on gray depth information. (a) Clustering result in original image. (b) Clustering result after median filtering denoising.

For the ISBI2015 public dataset, when the number of clusters takes $K \in (0, 25]$, the nuclei with similar positions and similar gray value lead to regions joined together, such as two nuclei in the red marker in Fig.7(b). When the number of clusters is greater than 35, i.e. $35 \leq K$, some nuclei and their surrounding areas cannot form a closed annular region after clustering, as shown in the red dots in the partially enlarged images in Fig. 7(c). When the number of clusters is within the range $K \in (25, 35)$, a regular closed annular region can be formed around the nucleus, for instance, Fig. 7(d) shows the experimental results when the number of clusters is $K = 30$.

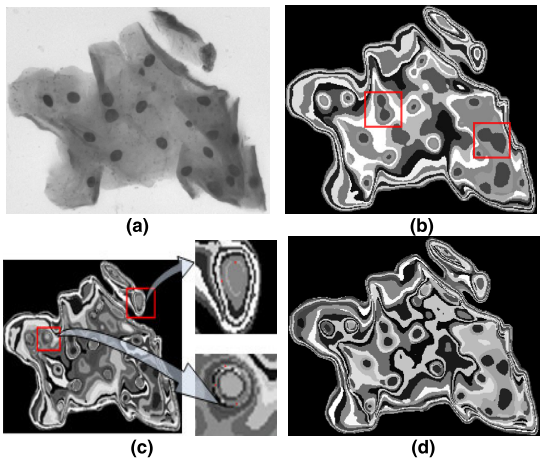

FIGURE 7. Clustering results for different clustering categories K. (a) Original image of the cell clump. (b) The clustering results when k is 20, in which the nuclei lead to regions joined together in the red markers. (c) The clustering result when k is 40, in which some nuclei and its surrounding areas cannot form a closed annular region after clustering in the red dot in the partially enlarged images. (d) The clustering results of k = 30.

2) CONSTRUCTING TREE DOMAIN

The tree domain structure is constructed by the annular regions in the clustering result according to their inclusion relationship. The whole cell clump regions are firstly designated as the root domain, and then each annular region is filled. According to the features of images on the ISBI2015 dataset, the areas of nuclei are larger than 50 pixels. When the filling area is larger than 50 pixels, it may be a nucleus region and is regarded as a subdomain of the root domain. Afterwards, compute the inclusion relationships among all subdomains to generate the parent–child relationship. Finally, a tree domain structure based on the annular regions can be obtained, as shown in Fig. 8.

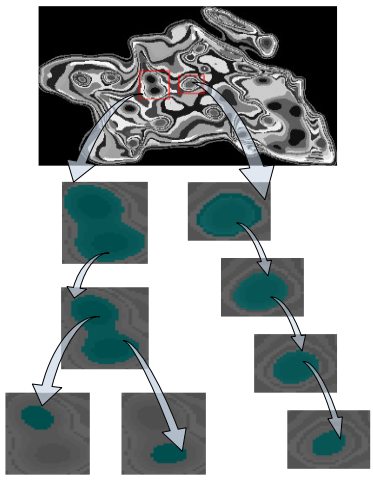

FIGURE 8. Tree domain of the annular region.

3) CANDIDATE NUCLEI SCREENING

In many cases, the gray value of the cytoplasm fluctuates greatly due to overlapping cells. Therefore, many noise

regions, which are small in area and different in shape, occur in the clustering results. The properties of each subdomain in the tree, such as area and solidity, are compared with the nucleus properties. The subdomains that have the similar nucleus properties are retained, others are deleted. Thus, a minimal tree domain is produced, and the computational complexity can be considerably reduced.

There may be multiple annular regions around the nucleus, so the minimal tree domain is traversed based on the depth-first strategy. The ''leaf'' subdomain that has one or more ''brother-node'' subdomains or the subdomain that has only one downward branch but has at least one ''brother-node'' subdomain is selected as candidate nucleus.

D. NUCLEUS FINE SEGMENTATION AND PSEUDO-NUCLEUS REMOVAL

Among the candidate nuclei, some nucleus contours are insufficiently accurate, and some are pseudo-nuclei. In this study, an iterative level set algorithm based on adaptive radius morphological dilation (ADLS) is proposed to perform the fine contour extraction and remove most of the pseudo-nuclei.

The level set function surface [37], [38] can be defined as (9),

$$\varphi(x, y, t) = \pm d' \tag{9}$$

where d' represents the distance from the point on the level set surface to the zero level. The contour curve satisfies (10).

$$\varphi(C(s, t), t) = 0 \tag{10}$$

The partial differential processing of (10) is as (11) and (12),

$$\varphi_t + \nabla\varphi \cdot C(s, t) = 0 \tag{11}$$

$$\nabla\varphi \cdot C(s, t) = 0 \tag{12}$$

where $\nabla\varphi$ is the gradient of the level set function φ. The unit normal vector of φ is expressed as (13).

$$n = -\frac{\nabla\varphi}{|\nabla\varphi|} \tag{13}$$

The φ evolution process satisfies (14),

$$\varphi_t + F|\nabla\varphi| = 0 \tag{14}$$

where F represents the velocity function. The target contour curve is obtained by (15).

$$\Gamma(t) = \{x|\varphi(x, y) = 0\} \tag{15}$$

The level set algorithm is a method for the evolution of spatial surfaces. Despite a topological change occurs in the evolution, it will not affect the evolution process. In the fine segmentation of the nucleus, the candidate nucleus topology may change. So, in this study, we use the level set method to perform the fine segmentation of the nucleus.

However, the iterative level set method usually recognizes the boundary which is close to the initialization curve. If the boundary obtained by rough segmentation is used as the initialization curve of the level set method, we have to employ a morphological dilation approach to further process the coarse segmentation boundary, which usually exists inside the nucleus. In a field of view, there are usually many cells. Because the size, shape and texture of the nuclei are different, the boundary of the coarse segmentation is often aside from its real nucleus boundary. A fixed radius morphological dilation algorithm cannot differentially dilate the coarse segmentation curve to an appropriate position for all the cells. Therefore, we combine the adaptive radius morphological dilation algorithm with the iterative level set to find the optimal dilation radius of each nucleus coarse segmentation boundary, so that a precise boundary of each nucleus can be achieved.

Firstly, compute the mean gray value of a candidate nucleus region in each plane of sample I, and find the focal plane that has the minimum mean gray value. Then perform morphological dilation operations on the candidate nucleus region at the focal plane found. Denote the original candidate nucleus region as bw, the dilation region $bw(i)$ is then obtained by (16), and the variance vector $\vec{S} = [s_1, s_2, \ldots, s_i]$ of the dilation region $bw(1), bw(2), \ldots, bw(i)$ is obtained by (17),

$$bw(i) = bw \oplus SE(i) \tag{16}$$

$$s_i = std(I. * bw(i)) \tag{17}$$

where i is the dilation radius, $\oplus$ is the morphological dilation operation, SE is the structural element with the dilation radius i, ''.*'' is the bitwise multiplication operation, and std is the variance operation.

The gradient vector $\vec{V} = [v_1, v_2, \ldots, v_i]$ of the boundary mirror extended $\vec{S}$ is defined as (18).

$$v_i = s_{i+1} - s_{i-1} \tag{18}$$

Three spatial relationships and variance curves existed between the candidate nucleus boundary and the nucleus are shown in Fig. 9.

1) When the candidate nucleus boundary contains nucleus, the variance vector curve is relatively flat, as shown in Figs. 9(a), (d).

2) When the candidate nucleus is contained in the nucleus, the variance vector exhibits an ''s''-shaped curve. When the candidate nucleus dilates in the nucleus, the gradient of the variance changes slowly and is a downward convex curve. The variance increases rapidly, when the candidate nucleus boundary intersects with the nucleus boundary. Afterwards, the variance curve tends to be flat and is an upward convex curve, as shown in Figs. 9(b), (e).

3) When an intersection exists between them, the variance vector curve is generally rising and then relatively flat, as shown in Figs. 9(c), (f).

Therefore, the point where the variance vector curve satisfies the convex condition and the absolute value of the gradient is the smallest is selected as the candidate nucleus dilation radius, as shown as (19).

$$r = \{r|s_r \geq \frac{s_{r-1} + s_{r+1}}{2} \text{and arg } \min_r |v_r|\} \tag{19}$$

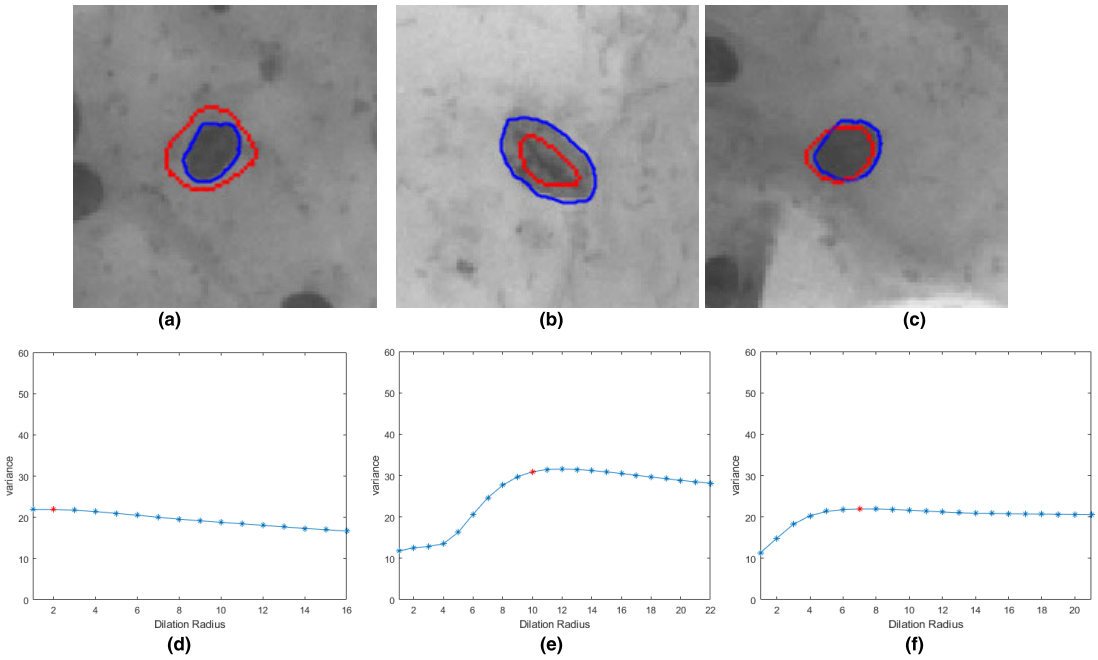

FIGURE 9. Three spatial relationships between candidate nuclei and nuclei and the variance curves. Three positional relationships between candidate nuclei and nuclei are shown in (a), (b) and (c) corresponding the containing, contained, and intersecting, respectively, where the red lines are the candidate nucleus boundaries and the blue lines are nucleus boundaries. Variance curves are shown in (d), (e) and (f) corresponding to the containing, contained, and intersecting relationships, respectively.

After the adaptive radius morphological dilation of the candidate nucleus boundary, the nucleus boundary can be accurately segmented by the iterative level set algorithm, and most of the pseudo nuclei can be removed. ADLS algorithm is shown in Algorithm 2.

III. EXPERIMENTS AND RESULTS

A. DATASET

The experimental samples in this study are based on the dataset published in the ''The Second Overlapping Cervical Cytology Image Segmentation Challenge'' organized by the IEEE International Biomedical Imaging Symposium. The dataset has a total of 17 samples, each of which contains 20 images of different depths in the same field of view, i.e., 20 different focal plane images in the same field of view. Each sample also includes an EDF image, in which each cell is focused. The image in the dataset is a gray image of size 1024*1024. Each sample contains approximately 40 cervical cells with different overlapping rate, contrast and texture. Eight samples in the dataset are defined as training dataset, and the training dataset is published nucleus and cytoplasm annotation images. The remaining nine samples are used as testing dataset, and only cytoplasm annotated images are published. Since this study is to investigate the nucleus segmentation of cervical cytology images, eight training samples are used as data for evaluating the performance.

Several measures such as the positive predictive value (*PPV*), negative predictive value (*NPV*) / sensitivity, harmonic average F between *PPV* and *NPV*, accuracy have been defined in [32], [39] as (20), (21), (22), and (23) respectively, to evaluate the results of nucleus segmentation,

$$PPV = TP/(TP + FP) \tag{20}$$

$$NPV = TN/(TN + FN) \tag{21}$$

$$F = 2^{*}(PPV^{*}NPV)/(PPV + NPV) \tag{22}$$

$$accuracy = (TN + TP)/(TN + TP + FN + FP) \tag{23}$$

where *TP* represents the number of pixels correctly predicted as positive, *FP* represents the number of pixels that are incorrectly predicted to be positive, *TN* represents the number of pixels correctly predicted as negative, and *FN* represents the pixel that is incorrectly predicted to be negative. A positive class indicates that the pixel is inside the nucleus, and a negative class indicates that the pixel is outside the nucleus.

B. RESULTS

The eight cervical cytology samples in the nucleus segmentation experiments were derived from the ISBI2015 training dataset. In Tables 1 and 2, our algorithms were compared with those of Lu *et al.* [23], Tareef *et al.* [19], and Phoulady *et al.* [4] in terms of object-based precision and recall measure. On the ISBI2015 training dataset, our procedure and Lu's procedure code provided in [23] were run on the same computer and software platform.

In terms of object-based precision and recall metrics, the experimental results from our method were quantitatively compared with the results obtained by Lu's method (Table 1). In eight cervical samples with a total of 320 nuclei,

Algorithm 2 ADLS Algorithm

Input: Candidate nuclei *cand_nucs*
Output: *Nuclei*
Set $A\_min = 100, A\_max = 800, Solidity = 0.95$, $iter\_in = 15$, $iter\_out = 2$, $alpha = 5$ and $lambda = 4$
1: **foreach** $cand\_nuc \in cand\_nucs$ **do**
2: $bw = get\_f(cand\_nuc)$% Get nucleus in focal plane
3: $bws = get\_dil(bw)$% Get dilation regions of nucleus
4: $[S, V] = cal\_s\_v(bws)$% Calculate S and V
5: % Calculate the optimal dilation radius
6: $r = cal\_opt\_r(S, V)$
7: % Update candidate nuclei as dilation region
8: $bw = update\ (bw, r)$
9: **while** 1 **do**
10: $nuc\_ref = ls(bw)$% Level set function
11: $area\_nuc = area(nuc\_ref)$% Get region area
12: $soli\_nuc = soli(nuc\_ref)$% Get region solidity
13: **if** $area(area\_nuc) < A\_max$ and $soli\_nuc > Solidity$ **then**
14: **if** $area(area\_nuc) < A\_min$ **then**
15: % mark the *nuc_ref* as a pseudo-nucleus
16: $nuclei\_pseu = pseudo\_nuc(nuc\_ref)$
17: **else**
18: % mark the *nuc_ref* as a nucleus
19: $Nuclei = nuc(nuc\_ref)$
20: **end**
21: break
22: **end**
23: **end**
24: **end**

TABLE 1. Results of our algorithm and that of lu in terms of Pre_{obj} and Rec_{obj}.

Algorithm	Cd	D	Pre_{obj}	Rec_{obj}
Lu [23]	250	310	0.806	0.781
Our	270	319	**0.846**	**0.844**

our algorithm detected 319 nuclei, of which the correct number was 270. The precision and recall were 0.846 and 0.844 respectively. Lu's algorithm could identify 310 nuclei, of which 250 were correctly detected; the precision and recall were 0.806 and 0.781 respectively.

In particular, the comparative experiments for cervical cytology sample numbered 017 on the ISBI2015 dataset were shown in Table 2. The object-based recall of our algorithm was higher than those of the other two methods reported by Tareef *et al.* [19] and Phoulady *et al.* [4]. On the basis of precision metrics, the result of our algorithm was the same as method of Tareef *et al.* [19] but higher than that of the algorithm of Phoulady *et al.* [4].

On the ISBI2015 public dataset, the comparative experiment results of our algorithm, Lu *et al.* [23], Li *et al.* [12], Ling *et al.* [21], Al-Kofahi *et al.* [34], and Song *et al.* [32] based on pixel metrics were shown in Tables 3 and 4.

TABLE 2. Results of our algorithm and those of tareef and phoulady in terms of Pre_{obj} and Rec_{obj}.

Algorithm	Cd	D	Pre_{obj}	Rec_{obj}
Tareef [19]	36	42	**0.97**	0.86
Phoulady[4]	34	45	0.91	0.76
Our	36	40	**0.97**	**0.89**

TABLE 3. Results of our algorithm and that of lu in terms of Pre_{pix}, Rec_{pix} and DC.

Algorithm	Pre_{pix}	Rec_{pix}	DC
Lu [23]	0.951(±0.061)	**0.935(±0.051)**	**0.941(±0.037)**
Our	**0.956(±0.06)**	0.919(±0.07)	0.934(±0.04)

TABLE 4. Results of our algorithm and those of four other algorithms in terms of PPV, NPV and F.

Algorithm	PPV	NPV	F
Li [12]	0.64	0.81	0.715
Zhang [21]	0.83	0.74	0.782
Yousef [34]	0.86	0.89	0.875
Song [32]	**0.95**	0.93	0.94
Our	0.91	**0.99**	**0.95**

The experimental results for pixel-based precision, recall and DC metrics were quantitatively compared (Table 3). As shown in Table 3, the proposed algorithm and Lu's algorithm obtained good results. The precision of our algorithm was 0.956, which was slightly higher than that of Lu's algorithm. On the basis of the pixel recall and DC, the experimental results obtained by our algorithm were 0.919 and 0.934, respectively; the values were slightly lower than those of Lu's algorithm (0.935 and 0.941, respectively).

In Table 4, the four algorithms of Li *et al.* [12], Zhang *et al.* [21], Al-Kofahi *et al.* [34], and Song *et al.* [32] were compared with our algorithm under three metrics: *PPV, NPV, F*. In terms of *NPV* and *F*, the results obtained by our method were 0.99 and 0.95, which were higher than those of the four other methods. The value of *PPV* in the current paper was competitive, as it was higher than those reported by Li *et al.* [12], Zhang *et al.* [21], and Al-Kofahi *et al.* [34], but slightly lower than that of Song *et al.* [32].

IV. DISCUSSION

A. COMPARISON AND ANALYSIS

The cell clump and approximate nucleus segmentation are two important parts of cervical nucleus segmentation process. In these two parts, the gray information of each position in the cervical cell sample was replaced with a depth information vector containing the gray values of the same position in all focal planes of the sample. Subsequently, the FCM clustering algorithm completed the segmentation of cell clumps with the number of clusters K = 3, and the segmentation of candidate nuclei with the number of clusters K = 30. Our algorithm could capture much comprehensive image information and obtain better nucleus detection results by using the depth

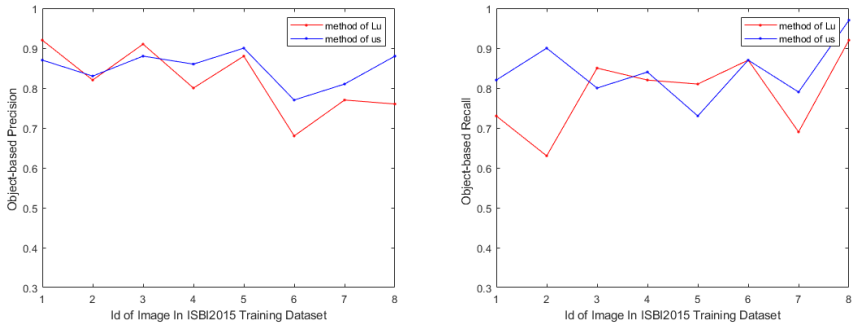

FIGURE 10. Compare the detection results of each sample on ISBI2015 training dataset by our and Lu's method. (a) Compare the detection results in object-based precision. (b) Compare the detection results in object-based recall.

information. As shown in Table 1, the object-based precision and recall metrics in the proposed algorithm were 4.7% and 7.5% higher than those of Lu's algorithm, respectively. In order to evaluate the nucleus detection performance of ours and Lu's method more objectively, we compared the detection results of each sample on the ISBI2015 training dataset.

We compared our method with Lu's method in terms of the detection results of each sample on the ISBI2015 training dataset. The object-based precision and recall in the second, fourth, sixth, and eighth samples of our algorithm were not lower than that of Lu's algorithm. For the first sample, the object-based recall of our algorithm was 11% higher than that of Lu's algorithm, but the object-based precision was lower than that of Lu's algorithm. The precision of our method was 2.2% higher than that of Lu's method, and the recall rate was 9.8% lower than that of Lu's method in the fifth sample. The Lu's method was slightly better than our algorithm in terms of precision and recall only in the second sample. Overall, our method demonstrated better performance than Lu's method in nucleus detection.

As shown in Fig. 11, the application of the depth information could segment nuclei with low contrast. The yellow regions in the first row of Fig. 11 were the correctly segmented nuclei of our method, but the Lu's algorithm did not correctly segment the nuclei.

In terms of pixel-based precision, recall, and DC metrics, the distribution of our nucleus segmentation result was shown in Fig.12. The pixel-based precision in 30% of the detected nuclei was more than 0.99, and that of only 1.5% was less than 0.75. The number of nuclei with pixel-based recall over 0.75 accounted for 97.4% of correctly detected nuclei by our method. As shown in Fig.12, the DC of all correctly identified nuclei of our method was more then 0.77, of which 44% of nuclei had a DC value greater than 0.95.

The nucleus segmentation performances of our and Lu's method were statistically analyzed with regard to pixel-based metrics on the ISBI2015 training dataset (Table 5). The percentages of nuclei with pixel-based precision reaching 0.8 and 0.9 were 97.4% and 90.4%, respectively, in the correctly detected nuclei; these values were higher than the

TABLE 5. Statistical analysis based on pixel metrics.

Algorithm	precision		recall		DC	
Range	>0.8	>0.9	>0.8	>0.9	>0.8	>0.9
Lu [23]	96.4%	88.8%	**97.6%**	**78.8%**	**98.4%**	**93.2%**
Ours	**97.4%**	**90.4%**	94.1%	71.9%	98.2%	84.8%

results reported by Lu. The proportions of nuclei with recall over 0.8 and 0.9 of our method were 94.1% and 71.9%, respectively, which were lower than those of Lu's method. In general, the pixel-based DC metric can better indicate the segmentation performance. Although the proportion of detected nuclei with DC higher than 0.9 was lower than that of Lu's algorithm, 84% of nuclei detected in our method had a DC value greater than 0.9. The proportion of DC over 0.8 was as high as 98%, that is, the DC of almost all detected nuclei was greater than 0.8. Our algorithm was inferior to Lu's method in terms of pixel-based recall and DC greater than 0.9. However our method had an advantage over pixel-based precision, and almost all the detected nuclei met the condition with DC more than 0.8. The accuracy and sensitivity of our method were 0.9952 and 0.9982, and those of the Lu's method were 0.9935 and 0.9977, respectively. We performed McNemar's test on the experimental results of the two methods, with $\alpha = 0.05$ as the statistically significant threshold. Since the P-value (<0.0001) was lower than our chosen significant threshold, we rejected the null hypothesis that the two model's performances are equal. The experimental results showed that the accuracy and specificity of our method are higher than those of Lu's method (P-value < 0.05).

The metrics such as *PPV*, *NPV*, *F* also could measure the performance of the boundary segmentation results. Table 4 showed that in terms of *PPV, NPV* and *F* our algorithm was higher than the methods in [12], [21] and [34], especially in *PPV*, which was higher than the other three methods by 23.5%, 16.8%, and 7.5%, respectively. Although the performance of our method based on *PPV* metrics in Table 4 was lower than that of the CNN method in [32],

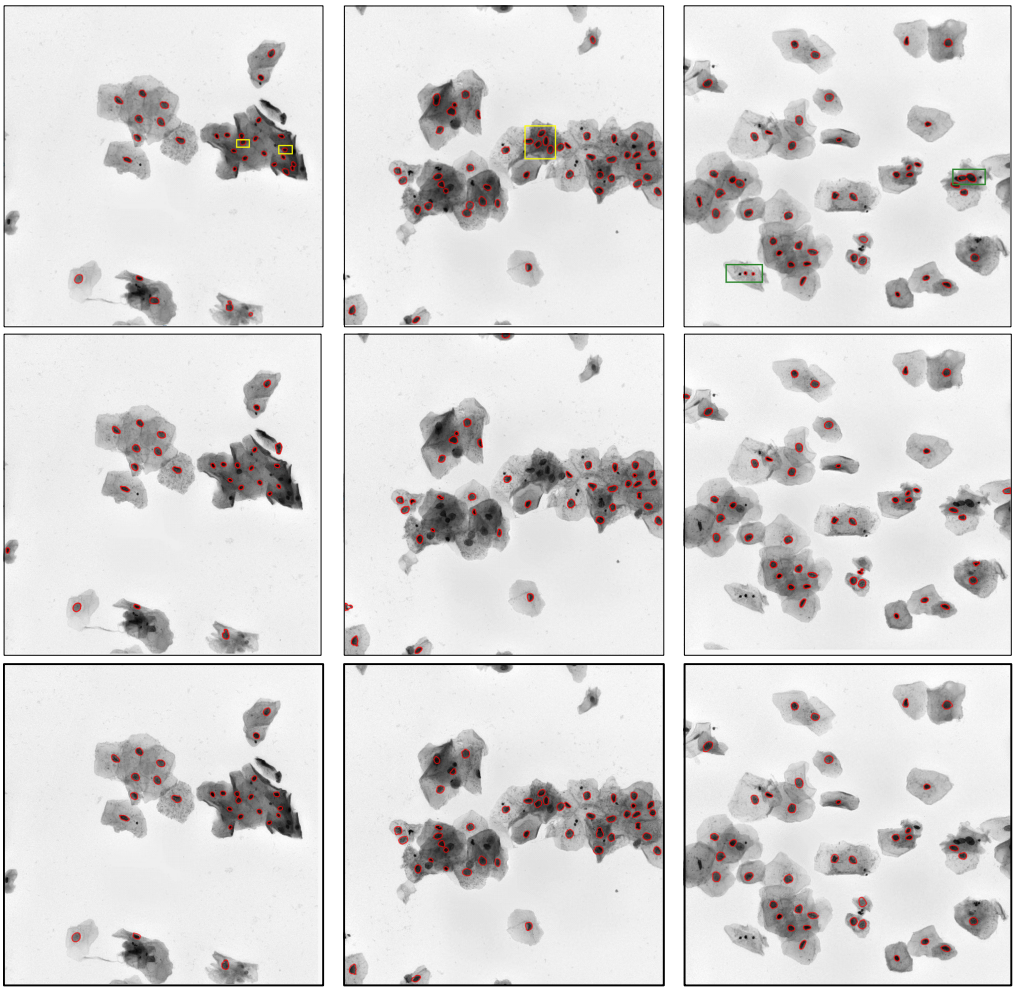

FIGURE 11. Nucleus segmentation results. From top to bottom: the annotated images, outlined by Lu [23], and the proposed method. The yellow regions in the first row were the correctly segmented nuclei, but the Lu algorithm did not correctly segment it. The green region was not correctly segmented by our and Lu's method.

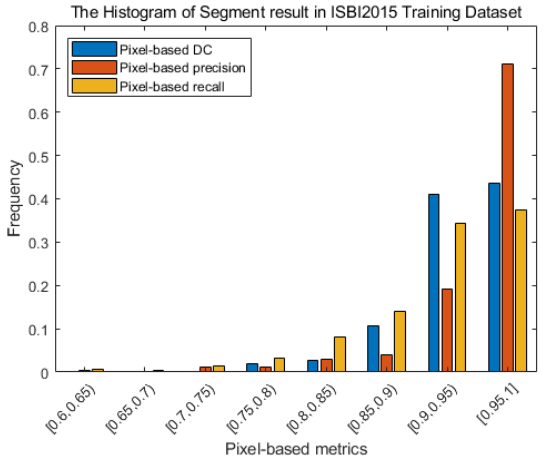

FIGURE 12. The distribution of pixel-based precision, recall, and DC metrics.

the value of NPV and F of our method were 6% and 1% higher than those of the latter, respectively.

In summary, not only can the combination of depth information and ADLS algorithm identify the nuclei more accurately, but also can accurately segment their boundaries.

B. COMPARISON OF FIXED AND ADAPTIVE RADIUS MORPHOLOGICAL DILATION APPROACHES

The coarse segmentation boundary, which was the level set initialization curve, was generally inside the nucleus. The iterative level set algorithm based on fixed radius morphological dilation (FDLS) approach dilated the nucleus regions according to the preset fixed radius, and it could not dilate the coarse segmentation curves of different nuclei to their own optimal positions, respectively. The adaptive radius morphological dilation approach adjusted its dilation radius according to the difference of each nucleus. Therefore, in our method, the adaptive radius morphological dilation approach was combined with the iterative level set method so as to obtain a precise nucleus segmentation boundary.

Different fixed radius morphological dilation combined with the iterative level set algorithm gave different

performances in Pre_{obj} and Rec_{obj}(Table 4). It was not easy to determine a relative better dilation radius such as 10 without stepwise searching. On the other hand, once the coarse segmentation algorithm parameters were adjusted, the performance of the fixed radius morphological dilation method decreased sharply, and the relative better dilation radius must be re-searched. As a contrast, the adaptive radius morphological dilation approach combined with the iterative level set algorithm adjusted its dilation radius adaptively according to the coarse segmentation boundary of each nucleus and obtained the best performance 0.85 and 0.80 in Pre_{obj} and Rec_{obj} respectively.

TABLE 6. Comparison of FDLS and ADLS.

Algorithm	FDLS						ADLS
Radius	4	6	8	10	12	14	--
Pre_{obj}	0.79	0.75	0.80	0.84	0.80	0.81	**0.85**
Rec_{obj}	0.53	0.67	0.79	0.84	0.79	0.74	**0.84**

C. COMPUTATIONAL COMPLEXITY

For large-scale, high-resolution cervical cytology sample images, the computational complexity was a challenge for all the segmentation algorithms. The computational complexity was high when the traditional segmentation methods were used to process the cervical cytology images with deep information. How to make full use of the information of different depth of images while maintaining moderate complexity of algorithm was one of the difficult problems that scholars tried to solve. In this study, we explored a novel approach to reducing the computational complexity for multi-depth focal images. As the first step of the proposed nucleus segmentation algorithm, we converted the three-dimensional data of cervical cytology samples with depth information into two-dimensional data images with only k values. The amount of data of the clustered two-dimensional image to be handled was significantly reduced, and the nucleus region met an annular feature. Then, the tree domain structure was constructed using these annular features to identify the nuclei.

In the experiments, a cervical cytology sample contained 20 focal-plane images, and the data volume was 20 times that of the single EDF image. All the experiments were completed in the following computational environment: Windows7 operation system, Intel (R) core i5-3470 processor, 12 GB memory, 500 G hard disk. We run the proposed method codes and Lu's method codes [23] separately on the Matlab R2018a platform. The experimental results showed that the proposed method handled the 20 focal-plane images and identified 258 nuclei in 960 seconds, with an average time of 3.7 seconds for a nucleus. The Lu's method handled the single EDF image and identified 248 nuclei in 252 seconds, with an average time of 1.02 seconds for a nucleus, let alone the time of generating the EDF image. Relatively speaking, the proposed method could obtain more accurate segmentation results with moderate computational complexity.

D. FURTHER WORK

Nucleus segmentation, as the first step of the CAD system, plays an important role in the cell detection and segmentation. The degree of nucleus atypia, such as nucleus enlargement, can reflect the abnormality of cells. The precise segmentation of nuclei implemented in our algorithm can ensure the exact extraction of nucleus area features. In the next step, we will continue to segment the cells located by the nuclei detected with the proposed algorithm in this paper and extract the lesion-related features of the nuclei and cytoplasm. On the basis of these extracted features, such as the nucleus area, and nucleus-to-cytoplasm ratio, the degree of abnormality of cells can be evaluated and provided to pathologists as evidence of cervical cancer. This process will reduce the work intensity of pathologist and increase the diagnostic accuracy of cervical cancer.

V. CONCLUSION

The nucleus segmentation of cervical cytoplasm images is a prerequisite for the computer-aided cervical cancer diagnosis. For the first time, the depth information in the cervical cytology images is used to segment the nuclei. The tree domain structure of the annular feature presented in the nucleus region after clustering is constructed to find those candidate nuclei. Furthermore, an iterative level set refinement segmentation algorithm based on adaptive radius morphological dilation is proposed to finely segment each candidate nuclei and remove the pseudo-nuclei. The experimental results show that the proposed nucleus segmentation algorithm for cervical smear images has high segmentation precision and a moderate computational complexity, especially for the case of poor contrast and overlapping cells.

REFERENCES

[1] J. Ferlay, I. Soerjomataram, R. Dikshit, S. Eser, C. Mathers, M. Rebelo, D. M. Parkin, D. Forman, and F. Bray, "Cancer incidence and mortality worldwide: Sources, methods and major patterns in GLOBOCAN 2012," *Int. J. Cancer*, vol. 370, no. 5, pp. 359–386, 2015, doi: 10.1109/ACCESS.2019.2919390.

[2] R. Catarino, "Cervical cancer screening in developing countries at a crossroad: Emerging technologies and policy choices," *World J. Clin. Oncol.*, vol. 6, no. 6, p. 281, 2015, doi: 10.5306/wjco.v6.i6.281.

[3] K. C. Santosh, L. Wendling, S. Antani, and G. R. Thoma, "Overlaid arrow detection for labeling regions of interest in biomedical images," *IEEE Intell. Syst.*, vol. 31, no. 3, pp. 66–75, May 2016, doi: 10.1109/MIS.2016.24.

[4] H. A. Phoulady, D. Goldgof, L. O. Hall, and P. R. Mouton, "A framework for nucleus and overlapping cytoplasm segmentation in cervical cytology extended depth of field and volume images," *Comput. Med. Imag. Graph.*, vol. 59, pp. 38–49, Jul. 2017, doi: 10.1016/j.compmedimag.2017.06.007.

[5] H. Lee and J. Kim, "Segmentation of overlapping cervical cells in microscopic images with superpixel partitioning and cell-wise contour refinement," in *Proc. IEEE Conf. Comput. Vis. Pattern Recognit. Workshops (CVPRW)*, Las Vegas, NV, USA, Jun. 2016, pp. 1367–1373.

[6] M. E. Plissiti, C. Nikou, and A. Charchanti, "Automated detection of cell nuclei in pap smear images using morphological reconstruction and clustering," *IEEE Trans. Inf. Technol. Biomed.*, vol. 15, no. 2, pp. 233–241, Mar. 2011, doi: 10.1109/TITB.2010.2087030.

[7] M. E. Plissiti, C. Nikou, and A. Charchanti, "Combining shape, texture and intensity features for cell nuclei extraction in pap smear images," *Pattern Recognit. Lett.*, vol. 32, no. 6, pp. 838–853, Apr. 2011, doi: 10.1016/j.patrec.2011.01.008.

[8] S. Tello-Mijares, "Abnormal cervical cell nuclei identification using Spatial-Context-Saliency regions and two-level cascade classifiers," *J. Med. Imag. Health Informat.*, vol. 9, no. 3, pp. 426–435, Mar. 2019, doi: 10.1166/jmihi.2019.2600.

[9] A. Husham, M. Hazim Alkawaz, T. Saba, A. Rehman, and J. Saleh Alghamdi, "Automated nuclei segmentation of malignant using level sets," *Microsc. Res. Techn.*, vol. 79, no. 10, pp. 993–997, Oct. 2016, doi: 10.1002/jemt.22733.

[10] M. Hu, X. J. Ping, and Y. H. Ding, "Automated cell nucleus segmentation using improved snake," in *Proc. Int. Conf. Image Process.*, Oct. 2004, pp. 2737–2740, doi: 10.1109/ICIP.2004.1421670.

[11] M. E. Plissiti, C. Nikou, and A. Charchanti, "Accurate localization of cell nuclei in PAP smear images using gradient vector flow deformable models," in *Proc. BIOSIGNALS*, 2010, pp. 284–289.

[12] K. Li, Z. Lu, W. Liu, and J. Yin, "Cytoplasm and nucleus segmentation in cervical smear images using radiating GVF snake," *Pattern Recognit.*, vol. 45, no. 4, pp. 1255–1264, Apr. 2012, doi: 10.1016/j.patcog.2011.09.018.

[13] M. S. Nosrati and G. Hamarneh, "Segmentation of overlapping cervical cells: A variational method with star-shape prior," in *Proc. IEEE 12th Int. Symp. Biomed. Imag. (ISBI)*, New York, NY, USA, Apr. 2015, pp. 186–189, doi: 10.1109/ISBI.2015.7163846.

[14] C. Chen, W. Wang, J. A. Ozolek, and G. K. Rohde, "A flexible and robust approach for segmenting cell nuclei from 2D microscopy images using supervised learning and template matching," *Cytometry A*, vol. 83A, no. 5, pp. 495–507, May 2013, doi: 10.1002/cyto.a.22280.

[15] C. Bergmeir, M. García Silvente, and J. M. Benítez, "Segmentation of cervical cell nuclei in high-resolution microscopic images: A new algorithm and a Web-based software framework," *Comput. Methods Programs Biomed.*, vol. 107, no. 3, pp. 497–512, Sep. 2012, doi: 10.1016/j.cmpb.2011.09.017.

[16] C. Jung and C. Kim, "Segmenting clustered nuclei using H-minima transform-based marker extraction and contour parameterization," *IEEE Trans. Biomed. Eng.*, vol. 57, no. 10, pp. 2600–2604, Oct. 2010, doi: 10.1109/tbme.2010.2060336.

[17] A. Gençtav, S. Aksoy, and S. Önder, "Unsupervised segmentation and classification of cervical cell images," *Pattern Recognit.*, vol. 45, no. 12, pp. 4151–4168, Dec. 2012, doi: 10.1016/j.patcog.2012.05.006.

[18] M. E. Plissiti, C. Nikou, and A. Charchanti, "Watershed-based segmentation of cell nuclei boundaries in pap smear images," in *Proc. 10th IEEE Int. Conf. Inf. Technol. Appl. Biomed.*, Nov. 2010, pp. 1–4, doi: 10.1109/ITAB.2010.5687745.

[19] A. Tareef, Y. Song, H. Huang, D. Feng, M. Chen, Y. Wang, and W. Cai, "Multi-pass fast watershed for accurate segmentation of overlapping cervical cells," *IEEE Trans. Med. Imag.*, vol. 37, no. 9, pp. 2044–2059, Sep. 2018, doi: 10.1109/TMI.2018.2815013.

[20] R. Saha, M. Bajger, and G. Lee, "Circular shape prior in efficient graph based image segmentation to segment nucleus," in *Proc. Digit. Image Comput., Techn. Appl. (DICTA)*, Dec. 2018, pp. 1–8, doi: 10.1109/DICTA.2018.8615768.

[21] L. Zhang, H. Kong, C. T. Chin, S. Liu, X. Fan, T. Wang, and S. Chen, "Automation-assisted cervical cancer screening in manual liquid-based cytology with hematoxylin and eosin staining," *Cytometry A*, vol. 85, no. 3, pp. 214–230, 2014, doi: 10.1002/cyto.a.22407.

[22] Z. Lu, G. Carneiro, and A. P. Bradley, "Automated nucleus and cytoplasm segmentation of overlapping cervical cells," in *Proc. Int. Conf. Med. Image Comput. Comput.-Assist. Intervent.* Berlin, Germany: Springer, 2013, pp. 452–460.

[23] Z. Lu, G. Carneiro, and A. P. Bradley, "An improved joint optimization of multiple level set functions for the segmentation of overlapping cervical cells," *IEEE Trans. Image Process.*, vol. 24, no. 4, pp. 1261–1272, Apr. 2015, doi: 10.1109/TIP.2015.2389619.

[24] S. Oprisescu, T. Radulescu, A. Sultana, C. Rasche, and M. Ciuc, "Automatic pap smear nuclei detection using mean-shift and region growing," in *Proc. Int. Symp. Signals, Circuits Syst. (ISSCS)*, Jul. 2015, pp. 1–4, doi: 10.1109/isscs.2015.7203961.

[25] S. Tello-Mijares, J. Bescós, and F. Flores, "Nuclei segmentation and identification in practical pap-smear images with multiple overlapping cells," *J. Med. Imag. Health Informat.*, vol. 6, no. 4, pp. 992–1000, Aug. 2016, doi: 10.1166/jmihi.2016.1750.

[26] S. Tello-Mijares and J. Bescós, "Region-based multifocus image fusion for the precise acquisition of pap smear images," *J. Biomed. Opt.*, vol. 23, no. 05, p. 1, May 2018, doi: 10.1117/1.JBO.23.5.056005.

[27] S. Tello-Mijares and F. Flores, "A novel method for the separation of overlapping pollen species for automated detection and classification," *Comput. Math. Methods Med.*, vol. 2016, May 2016, Art. no. 5689346, doi: 10.1155/2016/5689346.

[28] R. Saha, M. Bajger, and G. Lee, "Spatial shape constrained fuzzy C-Means (FCM) clustering for nucleus segmentation in pap smear images," in *Proc. Int. Conf. Digit. Image Comput., Techn. Appl. (DICTA)*, Nov. 2016, pp. 1–8, doi: 10.1109/DICTA.2016.7797086.

[29] R. Saha, M. Bajger, and G. Lee, "Circular shape constrained fuzzy clustering (CiscFC) for nucleus segmentation in pap smear images," *Comput. Biol. Med.*, vol. 85, pp. 13–23, Jun. 2017, doi: 10.1016/j.compbiomed.2017.04.008.

[30] K. C. Santosh and P. P. Roy, "Arrow detection in biomedical images using sequential classifier," *Int. J. Mach. Learn. Cybern.*, vol. 9, no. 6, pp. 993–1006, Jun. 2018, doi: 10.1007/s13042-016-0623-y.

[31] A. Tareef, Y. Song, W. Cai, H. Huang, H. Chang, Y. Wang, M. Fulham, D. Feng, and M. Chen, "Automatic segmentation of overlapping cervical smear cells based on local distinctive features and guided shape deformation," *Neurocomputing*, vol. 221, pp. 94–107, Jan. 2017, doi: 10.1016/j.neucom.2016.09.070.

[32] Y. Song, E.-L. Tan, X. Jiang, J.-Z. Cheng, D. Ni, S. Chen, B. Lei, and T. Wang, "Accurate cervical cell segmentation from overlapping clumps in pap smear images," *IEEE Trans. Med. Imag.*, vol. 36, no. 1, pp. 288–300, Jan. 2017, doi: 10.1109/TMI.2016.2606380.

[33] Z. Lu, G. Carneiro, A. P. Bradley, D. Ushizima, M. S. Nosrati, A. G. C. Bianchi, C. M. Carneiro, and G. Hamarneh, "Evaluation of three algorithms for the segmentation of overlapping cervical cells," *IEEE J. Biomed. Health Informat.*, vol. 21, no. 2, pp. 441–450, Mar. 2017, doi: 10.1109/jbhi.2016.2519686.

[34] Y. Al-Kofahi, W. Lassoued, W. Lee, and B. Roysam, "Improved automatic detection and segmentation of cell nuclei in histopathology images," *IEEE Trans. Biomed. Eng.*, vol. 57, no. 4, pp. 841–852, Apr. 2010, doi: 10.1109/TBME.2009.2035102.

[35] J. C. Dunn, "A fuzzy relative of the ISODATA process and its use in detecting compact well-separated clusters," *J. Cybern.*, vol. 3, no. 3, pp. 32–57, Jan. 1973.

[36] J. C. Bezdek, "Pattern recognition with fuzzy objective function algorithms," *Adv. Appl. Pattern Recognit.*, vol. 22, no. 1171, pp. 203–239, 1981, doi: 10.1007/978-1-4757-0450-1.

[37] C. Li, C. Xu, C. Gui, and M. D. Fox, "Distance regularized level set evolution and its application to image segmentation," *IEEE Trans. Image Process.*, vol. 19, no. 12, pp. 3243–3254, Dec. 2010, doi: 10.1109/TIP.2010.2069690.

[38] S. Osher and J. A. Sethian, "Fronts propagating with curvature-dependent speed: Algorithms based on Hamilton-Jacobi formulations," *J. Comput. Phys.*, vol. 79, no. 1, pp. 12–49, 1988, doi: 10.1016/0021-9991(88)90002-2.

[39] H. Kong, M. Gurcan, and K. Belkacem-Boussaid, "Partitioning histopathological images: An integrated framework for supervised color-texture segmentation and cell splitting," *IEEE Trans. Med. Imag.*, vol. 30, no. 9, pp. 1661–1677, Sep. 2011, doi: 10.1109/TMI.2011.2141674.

[40] A. P. Bradley and C. P. Bamford, "A one-pass extended depth of field algorithm based on the over-complete discrete wavelet transform," in *Proc. Image Vis. Comput. (IVCNZ)*, Akaroa, New Zealand, 2004, pp. 279–284.

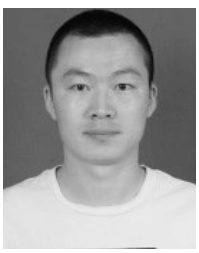

TAO WANG received the B.Sc. and M.Sc. degrees from the Harbin University of Commerce, in 2010 and 2013, respectively. He is currently pursuing the Ph.D. degree with the Harbin University of Science and Technology. His main research interests include image processing and pattern recognition.

JINJIE HUANG received the B.Sc. and M.Sc. degrees from the Harbin University of Science and Technology, in 1990 and 1997, respectively, and the Ph.D. degree from the Harbin Institute of Technology, in 2004. He is currently a Professor with the Harbin University of Science and Technology. His main research interests include intelligent control of complex industrial process, pattern recognition, and image processing.

DEQUAN ZHENG received the B.Sc. degree from Heilongjiang University, in 1991, and the M.Sc. and Ph.D. degrees from the Harbin Institute of Technology, in 1998 and 2006, respectively. He is currently a Professor with the Harbin University of Commerce. His main research interests include data mining, electronic commerce, and artificial intelligence.

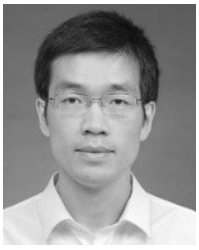

YONGJUN HE (Member, IEEE) received the B.S. degree in electrical engineering from the Harbin University of Science and Technology, Harbin, China, in 2003, and the M.S. and Ph.D. degrees from the School of Computer Science, Harbin Institute of Technology, Harbin, in 2006 and 2008, respectively. He is currently a Professor with the School of Computer Science and Technology, Harbin University of Science and Technology. His research interests include speech speaker recognition, machine learning, image processing, and speech processing.